ELSEVIER

DEM-based morphometry of range-front escarpments in Attica, central Greece, and its relation to fault slip rates[☆,☆☆]

Athanassios Ganas[a,*], Spyros Pavlides[b], Vassilios Karastathis[a]

[a]*Geodynamics Institute, National Observatory of Athens, P.O. Box 20048, Athens 11810, Greece*
[b]*Department of Geology, Aristotle University of Thessaloniki, Thessaloniki 54124, Greece*

Abstract

In this paper, we apply current geological knowledge on faulting processes to digital processing of Digital Elevation Models (DEM) in order to pinpoint locations of active faults. The analysis is based on semiautomatic interpretation of 20- and 60-m DEM and their products (slope, shaded relief). In Northern–Eastern Attica, five normal fault segments were recognized on the 20-m DEM. All faults strike WNW–ESE. The faults are from west to east: Thriassion (THFS), Fili (FIFS), Afidnai (AFFS), Avlon (AVFS), and Pendeli (PEFS) and range in length from 10 to 20 km. All of them show geomorphic evidence for recent activity such as prominent range-front escarpments, V-shaped valleys, triangular facets, and tilted footwall areas. However, escarpment morphometry and footwall geometry reveal systematic differences between the "external" segments (PEFS, THFS, and AVFS) and the "internal" segments (AFFS and FIFS), which may be due to mechanical interaction among segments and/or preexisting topography. In addition, transects across all five escarpments show mean scarp slope angles of $22.1° \pm 0.7°$ for both carbonate and metamorphic bedrock. The slope angle equation for the external segments shows asymptotic behaviour with increasing height. We make an empirical suggestion that slope angle is a function of the long-term fault slip rate which ranges between 0.13 and 0.3 mm/yr. The identified faults may rupture up to magnitude 6.4–6.6 earthquakes. The analysis of the 60-m DEM shows a difference in fault patterns between Western and Northern Attica, which is related to crustal rheology variations.
© 2004 Elsevier B.V. All rights reserved.

Keywords: Morphometry; DEM; Normal faults; Scarp; Slope; Attica; Central Greece

1. Introduction

Many workers have used Digital Elevation Models (DEM) to observe and map landforms and structural boundaries, and to display and to understand spatial relationships of structures (e.g., Murphy, 1993; Wdowinski and Zilberman, 1997; Goldsworthy and
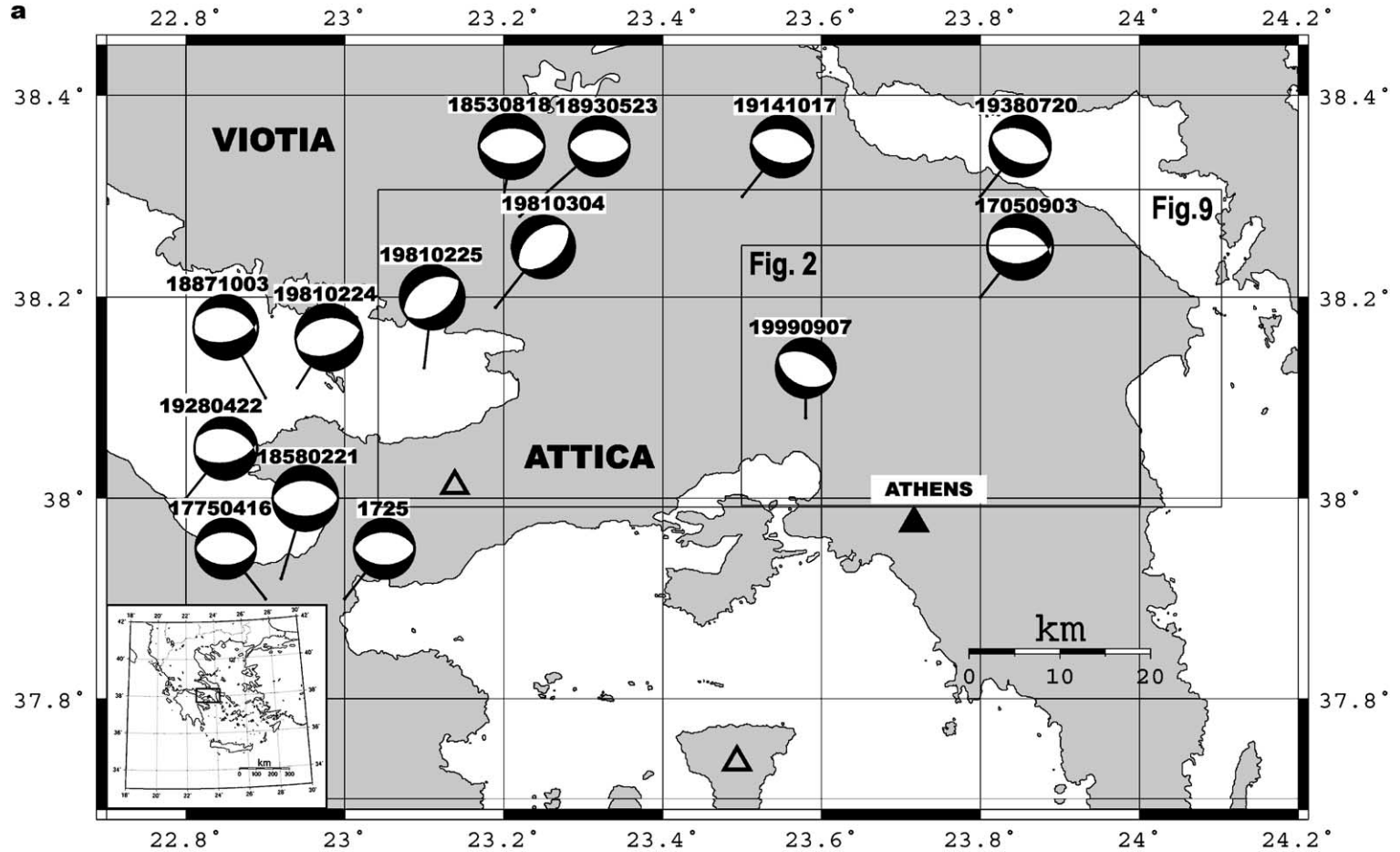
Fig. 1. (a) Map of Attica and surrounding areas with superimposed seismicity pattern of the last 300 years. Beachballs represent focal mechanisms of large earthquakes, with black colour indicating the compressional quadrant. Note that seismicity is concentrated at the eastern end of the Gulf of Corinth and inside the Thiva basin. Focal mechanism data are compiled from Ambraseys and Jackson (1997, 1998); Papadopoulos (2000); and Taymaz et al. (1991). Open triangles indicate Quaternary volcanic centres. Black triangle shows location of Athens historic centre. (b) Oblique view of a Landsat satellite image of Attica, central Greece, showing main physiographic features including mountain ranges (dark gray areas), marine gulfs (black areas), and sedimentary basins (light gray areas). Image dimensions: 120 km along E–W, 60 km along N–S.
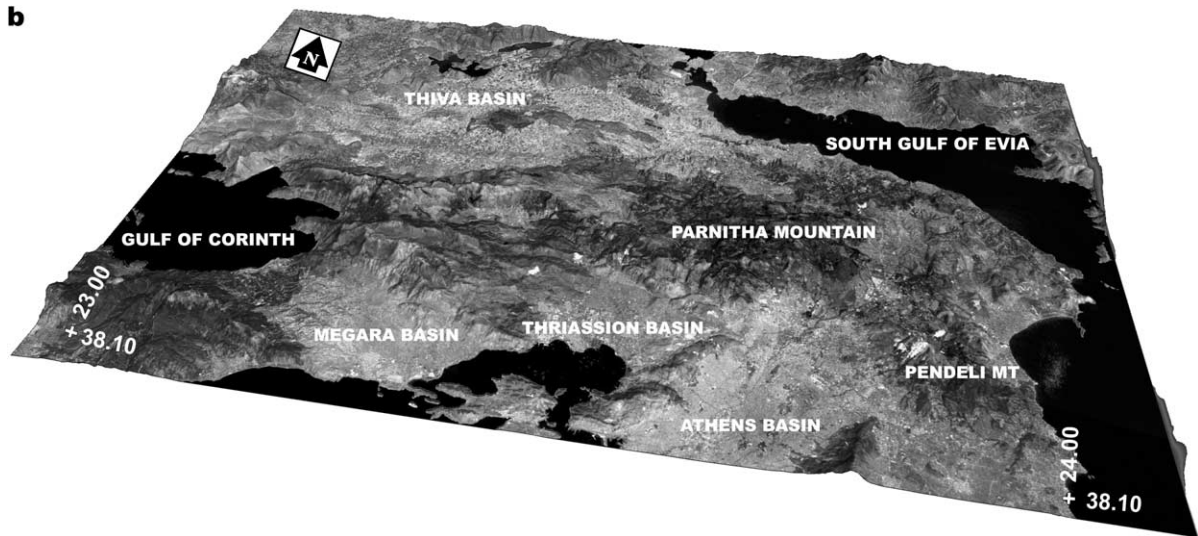
Fig. 1 (*continued*).

Jackson, 2000; Ganas et al., 2001; Michetti et al., 2001; Vysotsky et al., 2002; Jordan et al., 2003). During recent years, a number of studies have established strong links between topography and crustal deformation by faulting: (a) elevation data are a key element in modeling fault growth and fault segmentation (e.g., Menges, 1990; Duncan et al., 2003); (b) in central Greece (Leeder and Jackson, 1993; Armijo et al., 1996; Ganas, 1997; Roberts and Ganas, 2000; Ganas et al., 2004) and in other rift systems such as the Basin and Range (Jackson and Leeder, 1994), normal fault scarps are located at the base of mountain fronts; (c) inside rift systems, topography can be used as a proxy for fault displacement (e.g., Anders and Schlische, 1994; Roberts and Ganas, 2000); (d) systematic variations of fault throw are correlated to topographic variations of the footwall (e.g., Roberts et al., 2002). These observations provide important constraints for the structural interpretation of DEM.

Attica is located within an extensional domain of the Aegean where normal faulting predominates (Ambraseys and Jackson, 1990; Ganas et al., 2004). The area was affected by the 7/9/1999 Athens earthquake (Fig. 1; Ms5.9; Papadopoulos et al., 2000), and recent field work (Pavlides et al., 2002) has indicated that rupture occurred along the Fili (Phyle) fault segment, a 8–10-km-long structure located in Parnitha Mountain to the NW of Athens (Figs. 2 and 3). Ganas et al. (2001) demonstrated that this normal fault is clearly seen in shaded relief imagery. Furthermore, Ganas (2002) presented a set of methods to identify normal fault segments using DEM. In this paper, we combine the digital processing techniques of Ganas et al. (2001) and Ganas (2002) with measurements on scarp morphometry and kinematics to show that DEM analysis may be used to characterize four other segments in Attica as active. We confirm our DEM-based structural mapping by the recent field work data in Attica (Pavlides et al., 2002; Ganas et al., 2004).

Our approach uses digital processing of DEM to pinpoint locations of active faults. We use the term active faults to describe faults capable of producing surface breaks during large earthquakes. In addition, we use the term fault segment in its geological sense; that is, a crustal-scale structure defined by decreasing displacements at both tips (Ganas, 1997; Roberts and Ganas, 2000). We suggest that digital processing of elevation data may provide information on (a) lengths of faults, (b) scarp heights and throws, and (c) relative degree of fault activity within the rift system. In order to extract information on fault activity, we employ several image processing techniques: (a) artificial illumination of DEM producing shaded relief images, (b) perspec-
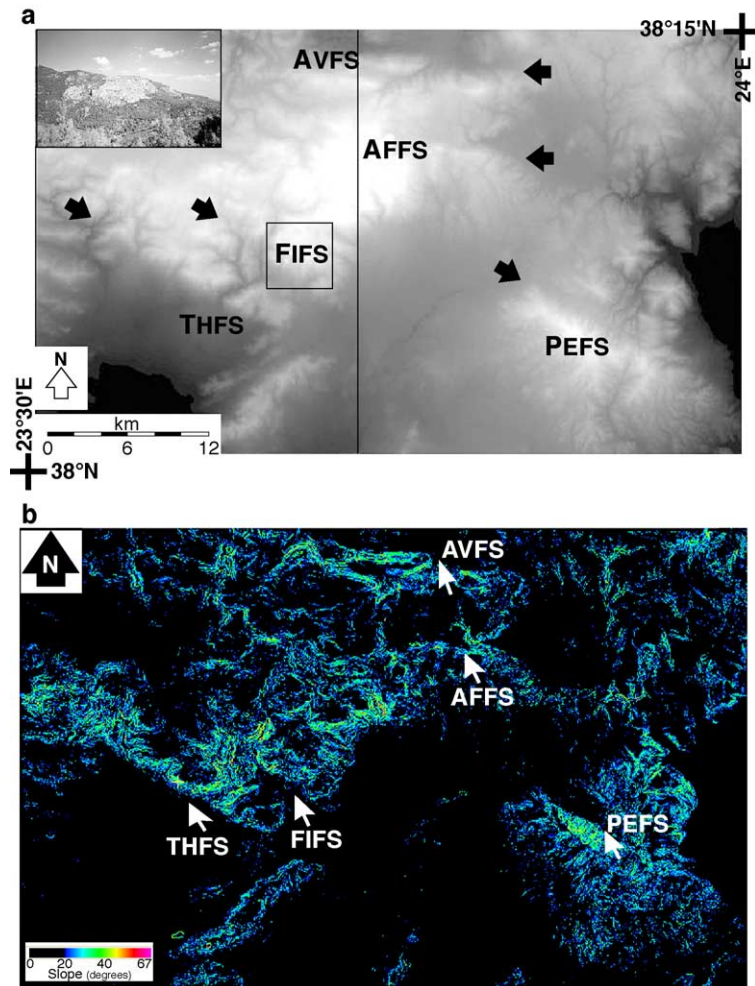
Fig. 2. (a) DEM intensity image mosaic showing elevations of Northern Attica, Greece. High elevations are shown as bright pixels, while low elevations as dark. Thin black line in centre is the mosaic stitch line. THFS is Thriassion Fault, FIFS is Fili Fault, AVFS is Avlon Fault, AFFS is Afidnai Fault, and PEFS is Pendeli Fault. Black arrows point to the termination of normal faults. Black box indicates extent of Fig. 3, respectively. Inset: field photograph of the Fili Fault Segment, Attica, Greece (September 2001). The fault strikes N120°E and dips 70° to the southwest. Notice the elliptical shape of the footwall. View is to the east. (b) Slope map of top image. Areas in black have slope angles less than 20°. White arrows indicate mountain fronts. Initials refer to name of fault segments.

tive-viewing of DEM, (c) along-strike profiling of mountain ranges, (d) cross-strike profiling of mountain ranges, and (e) profiling of slope maps. Then, we use the extracted information in order to (a) calculate maximum earthquakes on fault segments and (b) compare the population of normal faults to the neighbouring Corinth Rift, an area of high extensional strain in Quaternary times (Armijo et al., 1996).

2. Geology

North and East Attica are dominated by the high mountains of Parnitha and Pendeli that are bounded by shallow, NW–SE, and NE–SW basins of Neogene age (Fig. 1b; Freyberg, 1951; Mettos et al., 2000). The basins are oriented obliquely to the current extension direction in central Greece (N–S±10°, Clarke et al., 1998) and show no evidence for earthquake rupturing
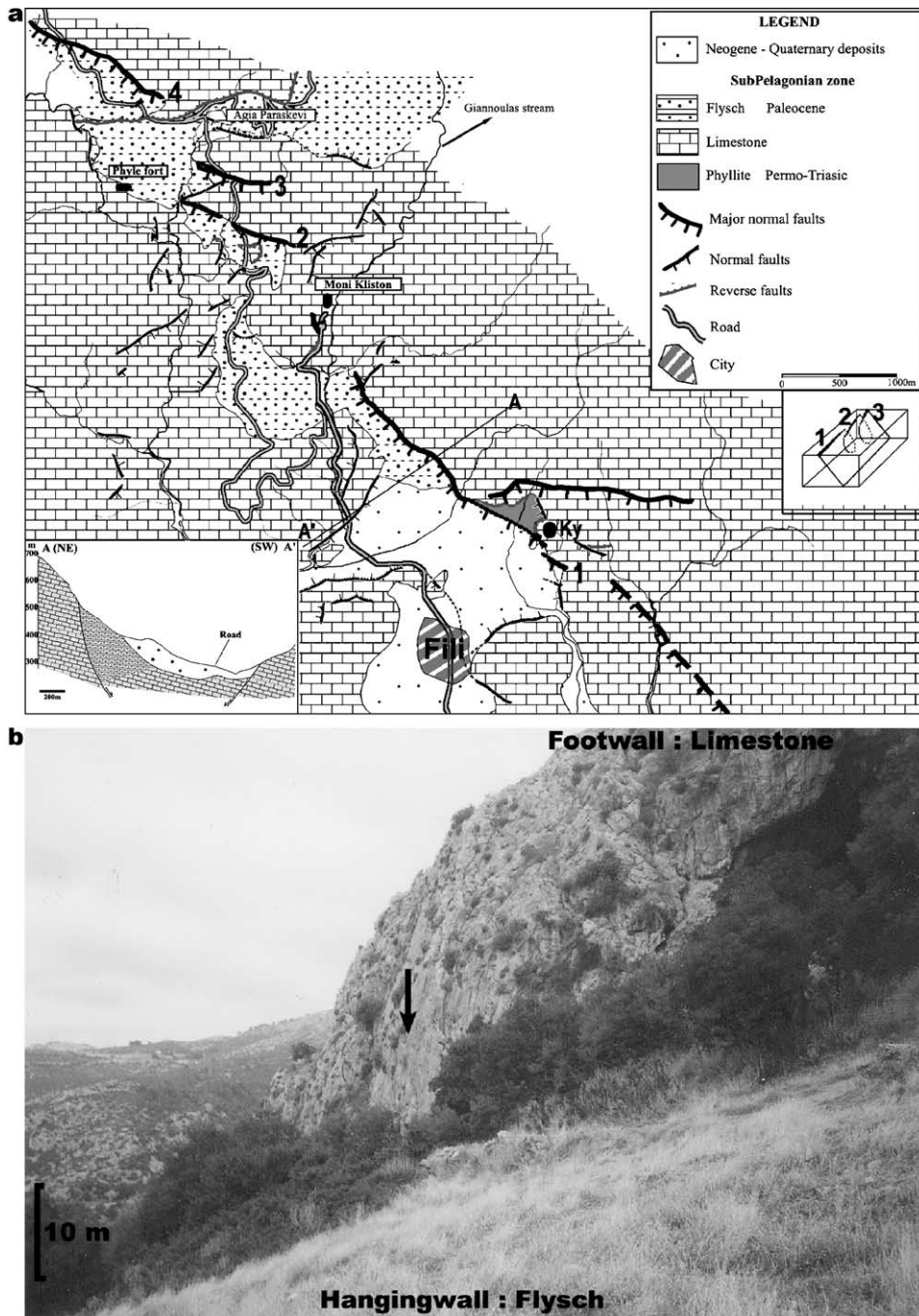
Fig. 3. (a) Geological map of the Fili Fault area, Attica, Greece. Thick black line is the FIFS identified in the previous figure (teeth on the downthrown block). Arabic numbers indicate smaller fault segments. Box at lower left shows cross-section AA′. A field photograph of the intersection of AA′ with the fault scarp is shown in panel (b). Inset cartoon shows segment linkage at depth (not to scale). Map after Ganas et al. (2004). (b) Field photograph (January 2000) of the large escarpment along the Fili Fault segment. View to the west.

during the last 2500 years (Ambraseys and Jackson, 1998). Both, historical and instrumental data for the area within 30 km from the epicentre of the 1999 event (38.08°N, 23.58°E) show no large earthquakes for the period 1700–2000, with the exception of the 1705 event (Fig. 1a). Ambraseys and Jackson (1997) and Goldsworthy and Jackson (2002) both located the epicentre of the 1705/09/03 (M 6.5) event on the northeastern flanks of Parnitha Mountain.

The prerift rocks of Parnitha mainly belong to the Subpelagonian isopic zone of the internal Hellenides. This carbonate platform was developed to the west of the Pelagonian microcontinent (Robertson et al., 1991). The carbonate rocks are neritic facies spanning the period from Triassic to Lower Cretaceous. An early deformation phase occurred during the Lower Cretaceous with the emplacement of an ophiolitic suite (Katsikatsos, 1977). Large ophiolitic bodies outcrop within the Subpelagonian rocks together with typical mélange formations as well as chert. The basement consists of Lower Palaeozoic gneisses, mica schists, amphibolites, and marble intercalations (Katsikatsos et al., 1986). The Subpelagonian rocks have been thrust to the east and southeast on top of the Attico–Cycladic, metamorphic Massif (Pendeli area) during Early Tertiary times. Syn-rift rocks include lacustrine marls and marly limestones, sandstones, fluvial conglomerates, and unconsolidated deposits (Mettos et al., 2000).

3. Data processing

In order to map fault segments accurately, we produced a 20-m DEM mosaic. The mosaic represents an area 42 km E–W by 27 km N–S (Fig. 2). Then, we used a 60-m DEM in order to apply our analysis on a larger area (Attica and Viotia; Fig. 1). The elevation data originated from the digitization of elevation contours of the general use maps of the Hellenic Army Geographical Service (1978, 1988, 1992) (HAGS) at scales 1:50,000 (sheets "Elefsis" and "Kifissia") and 1:250,000 (sheet "Khalkis"). Both planimetric and elevation accuracy is well within the requirements for fault segment mapping. The map specifications report vertical accuracy as a fourth of the contour interval, which is 20 m for the 1:50,000 scale and 100

m for the 1:250,000, respectively. So, vertical accuracy is 5 m for the 1:50,000 map and 25 m for the 1:250,000, respectively. Because of the multiplicative nature of errors involved in digital processing of elevation data (digitization of contours, georeferencing using a polynomial transformation, interpolation between contours), it is probable that there may be few places where larger errors in the vertical (z) dimension exist, although we did not compared our dataset to an external one. However, one recent investigation on similar pixel size and origin DEM (30-m USGS; Holmes et al., 2000) reports mean z-errors of 0.1 m with a standard deviation of 4.7 m, so we estimate a similar z-error for our data set.

The working procedure involved (a) scanning of HAGS maps in A0 size; (b) georeferencing of HAGS maps by a 1st-order polynomial transformation using the GEOMATICA™ software; (c) on-screen digitization of contours and mountain peaks; (d) constructing a mosaic of contours of both maps along the 23° 45′ meridian; (e) encoding of the values of digitized contours onto an empty 16-bit channel; and (f) building of the DEM in grid format using interpolation inside the ORTHOENGINE™ software suite and calculation of DEM derivatives (slope, shaded relief, etc.). The extraction of a slope profile across the mountain front was done by creating individual line–vector layers on the 20-m raster layer (Fig. 2b) and sampling those vector layers by reading both the elevation and the slope value beneath them, using the algorithm VSAMPLE. Each profile results was exported to an ASCII file. The slope data were then processed with a standard statistical package.

The 60-m DEM was produced by on-screen digitising of elevation contours of the 1:250,000 map sheet "Khalkis". Auxiliary elevation information was available by use of spot heights (mountain peaks) and river courses (converging elevation minima), so that the final grid model was constructed at 60-m spacing by a kriging interpolator. The 60-m DEM smoothes topography more than the 20-m one because the contour interval is larger. However, the long wavelength features of topography (mountain ranges and valleys) remain clear. Using this data set, we were able to map a dozen normal fault segments which document a profound difference in terms of strain localization when compared to active structures to the west (Gulf of Corinth).

4. Data analysis and interpretation methods

4.1. Image tone

The first property of an elevation image is the tonal variation of pixels usually spread out on a 16-bit scale (0–65535 m). The convention is to use a normal look-up table for heights, i.e., increasing brightness levels correspond to higher elevations. It follows that continuous linear tonal boundaries on the intensity image for distances more than 100 pixels (or 2 km on the ground) indicate the positions of mountain fronts (see Fig. 2a). Some times, the tonal boundaries are quite sharp; that is, the values of pixels on either side can differ by more than 500 m depending on DEM resolution. Their image locations can be easily matched with long breaks in slope (seen in computed slope maps; Fig. 2b) and are assumed to indicate the positions of fault scarps, which in turn indicate long-term neotectonic deformation (hundred thousand to several millions of years). This piece of evidence can be compared to lineaments observed on winter satellite imagery where we make use of the low sun angle to locate large structures (Salvi, 1995; Ganas, 1997; Goldsworthy and Jackson, 2000).

In Fig. 2a, we show five such areas where tonal boundaries are sharp and imposing. After locating the rapid tone change, we measure the distance along which this change is significant, i.e., more than a few times the contour interval. This method supplies lineaments along which elevations decrease system-atically until they merge with the flat area of the DEM. An additional criterion is provided by geology and is related to the lineament's orientation with respect to the current extension direction (N–S), as active normal faults are located at right angles to extension. One of those selected areas (inset box in Fig. 2a) has been confirmed to represent a large normal fault by both Pavlides et al. (2002) and Ganas et al. (2004). This is the Fili Fault segment located on the south flanks of Parnitha Mountain (FIFS; Fig. 3; note Fili is referred to as Phyle in archaeological literature). The 20-m DEM has reproduced both actual location of the scarp (Fig. 3b) and the scarp height. In addition, our 11-km estimate for this segment is close to what has been determined from geological data (10 km; Pavlides et al., 2002). It is reasonable to suggest that the other four DEM, features identified in Fig. 2a,

correspond to active normal faults. We elaborate further on this below.

4.2. Image derivative: slope

The first derivative of elevation is the slope angle. Abrupt changes in slope across the landscape are indication of active faulting (e.g., Sanders and Slemmons, 1996; Hooper et al., 2003), and lineaments seen in slope maps may represent fault scarp localities. We have calculated the slope map for Attica (Fig. 2b), using the algorithm embedded in GEOMATICA. The algorithm calculates the surface slope for each pixel of an elevation channel (see Appendix A for details). Slope at a point is calculated as the slope of the plane formed by the vector connecting the left and right neighbours and the vector connecting the upper and lower neighbours of the pixel. The output image contains slope values which range from $0°$ to $90°$.

On the Attica slope map, we observe that a linear break in slope angles exists that has a value of around $20°$. This is manifested by the black to green colour transition in Fig. 2b. We also note that this systematic break in slope angles matches the elevation change across the tonal lineaments identified in the previous section. Using this method, we observe that there are five areas where the terrain lineaments (a) are longer than 10 km, and (b) both elevation and slope angle decrease towards their ends. We suggest that their origin is attributed to normal fault activity as opposed to river terracing or bedrock erosion. A recent drainage analysis of Parnitha Mountain by Mariolakos et al. (2001) reports mainly N–S stream directions, which are across the lineaments detected in our slope maps.

4.3. Artificial illumination-shaded relief

The DEM were processed so that shaded relief images were produced using various illumination conditions in order to study the long-term evolution of landforms in Northern Attica. The algorithm employs a user-specified light source to convert an elevation channel to a shaded relief image. The shaded grey level at a point (pixel) is calculated as the cosine of the angle between the normal vector to the surface and the direction of illumination, scaled to the range of 0–255. All surfaces not illuminated by the
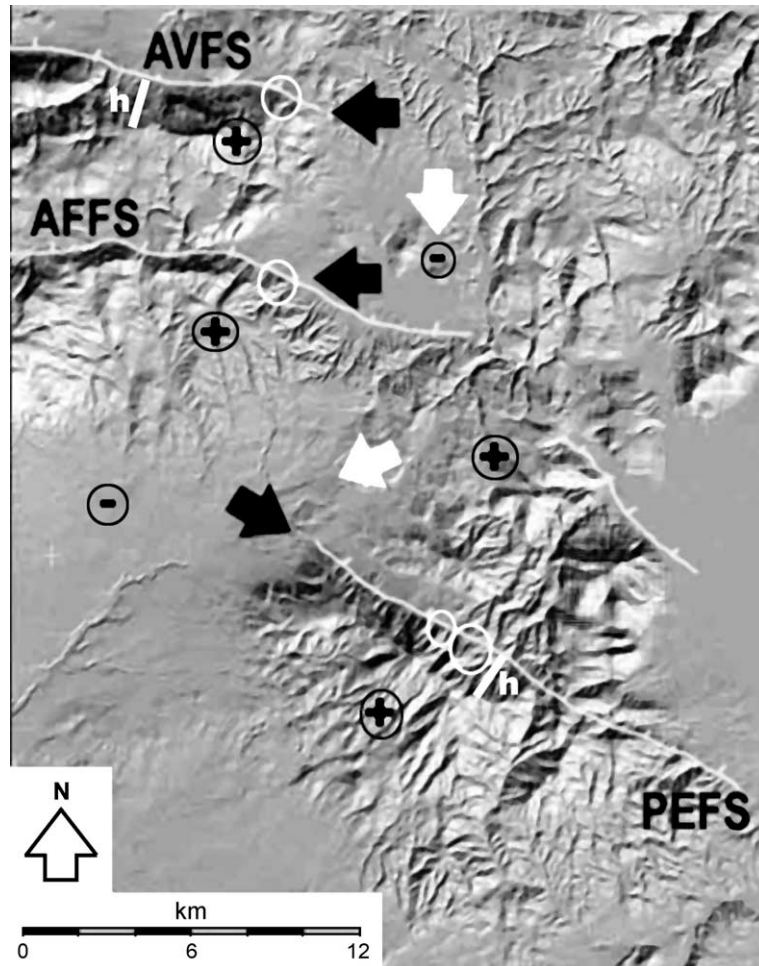
Fig. 4. Shaded relief image of the right patch of the 20-m DEM. Illumination is from the southeast at a low angle to accentuate topography. Thin white lines with ticks show normal fault trace with downthrown side. Thick white bars (labeled h) indicate limit of axial channels that flow across the fault line. White circles point to faceted slopes along the mountain front. Black arrows show fault terminations. White arrows indicate average flow direction of streams. Arithmetic signs indicate uplift (+) and subsidence (−), respectively. AVFS—Avlon Fault Segment; AFFS— Afidnai Fault Segment; PEFS—Pendeli Fault Segment.

light source (i.e., angle greater than 90° or a negative cosine) are set to 0. Our illumination conditions are oriented as follows: assuming that a line is drawn connecting the point source to the top left pixel of the image, the azimuth angle is the azimuth of this line in degrees clockwise from north (top of the image); the elevation angle is the elevation of the line in degrees from the horizontal.

From shaded relief, we can visualize footwall geomorphology along strike of major faults (Leeder and Jackson, 1993; Pike, 2000; Ganas et al., 2001; Ganas, 2002; Oguchi et al., 2003). The shaded relief

image in Fig. 4, simulating a low sun angle (elevation=25° or zenith=65°), SE-viewing direction (from N140°E) can be used as a raster background to digitize large active faults. Following from Fig. 2, in Fig. 4, we can trace four major faults (thin white lines), and we can infer their dip direction (towards N10–30°E) because there are numerous north-trending valleys that terminate abruptly against a flat plain. The existence and parallel arrangement of the footwall valleys are inferred by the linear shape of the shadows. Many localities along the mountain fronts display triangular facets, a geomorphic feature char-

acteristic of normal fault activity (e.g., Menges, 1990; Leeder and Jackson, 1993; Jackson and Leeder, 1994).

We note that the Pendeli Fault-PEFS footwall is more incised than both Avlon-AVFS and Afidnai-AFFS footwalls. This is manifested by the number of footwall valleys along strike (Fig. 4) and is probably due to lithological differences of the prerifted basement. Hard limestone exist to the west, while marbles and (softer) schists exist to the east (Katsikatsos, 1977; Katsikatsos et al., 1986). However, the distance from the fault trace to the mountain crest line ("hinterland" extent) along all three faults imaged in Fig. 4 does not exceed 2.5 km. This area is drained by axial channels that flow across the fault line, and this distance is almost equal for segments AVFS and PEFS (Fig. 4, see letter h). Given the same climatic conditions over the Quaternary period for those faults, this geomorphological observation points to similar footwall erosion rates for both, otherwise, the hinterland extent would be different for individual faults. If this is true, then, we may infer that similar footwall uplift rates occur along these normal faults, therefore, similar slip rates may be assumed. Furthermore, faults AVFS, AFFS, and PEFS are spaced 6–8 km across-strike, an amount that suggests early stages of rifting (Cowie and Roberts, 2001).

A second major use of the shaded relief is the extraction and study of drainage patterns. In the upper part of Fig. 4, we observe rectilinear features with lengths of 1–6 km incised into the landscape. These features represent streams arranged in a dendritic pattern which forms where the surface is relatively flat and a homogeneous subsurface geology exists. We suggest that the streams have southern flow directions because they drain the footwall area of all three fault segments (Avlon, Afidnai, and Pendeli) in agreement with block tilting due to uplift. We note that uplift of crustal blocks in the area is also reported by geophysical data (Metaxas et al., 2001). In particular, the southern stream courses at the ends of segments AVFS and AFFS indicate tilt due to an NW–SE striking coastal fault further to the North. This interpretation is in agreement with the recent work of Goldsworthy and Jackson (2002), where normal faulting is reported along the Northern Attica coastline. Axial streams have developed on the hanging wall of both AVFS and AFFS but with opposite flows (west for AVFS

and east for AFFS). No axial drainage exists in the hanging wall of the Pendeli segment because a younger normal fault (noted by a thin line) has developed some 8 km to the north. It is probable that this young fault links to the Afidnai segment (AFFS).

4.4. Profiling

A frequent use of a DEM image is that longitudinal profiles of mountain ranges can be extracted to display how topography varies along strike. Profile extraction is semiautomatic because the data are in raster, grid format with northing, easting, and elevation values for each sampled point. In our study, the profiles have been selected along lines very close to the actual crest lines of the ranges because we are not interested in absolute values but on footwall geometry. They are shown in Fig. 5. The young age of the landforms is evident from the V-shaped river valleys in profiles AA′, BB′, and DD′. However, we note the marked difference in the profile shape between the large segments (Thriassion, Avlon, and Pendeli) as opposed to the small segments (Fili and Afidnai). Given the similar lithology of Mt. Parnitha rocks, we suggest that the footwall asymmetry is due to a combination of (a) preexisting topography and (b) fault interaction (e.g., Roberts et al., 2002) between the inner faults (FIFS and AFFS) and the faults that define the present-day mountain front (THFS and AVFS). Field mapping in Parnitha by Ganas et al. (2004) showed the existence of fault planes with a NE–SW orientation and dip to the SE, i.e., normal to the WNW–ESE segments mapped on the DEM. It is probable that the NE–SW planes represent a former phase of extension, which is also associated with topography built-up.

Another technique is to draw transverse profiles (Fig. 5) to locate significant breaks and measure escarpment heights. All large segments are associated with high relief (Table 1) and have escarpment heights between 76 and 416 m (Table 2). We note that the position of two of the range-front escarpments on DEM imagery (Thriassion, Avlon; Fig. 6) roughly coincides with large normal offsets within the Attica upper crust, as has been imaged in seismic tomography by Drakatos et al. (2002). This supports our interpretation that both structures reach seismogenic depths (10–15 km). If we accept the notion that both
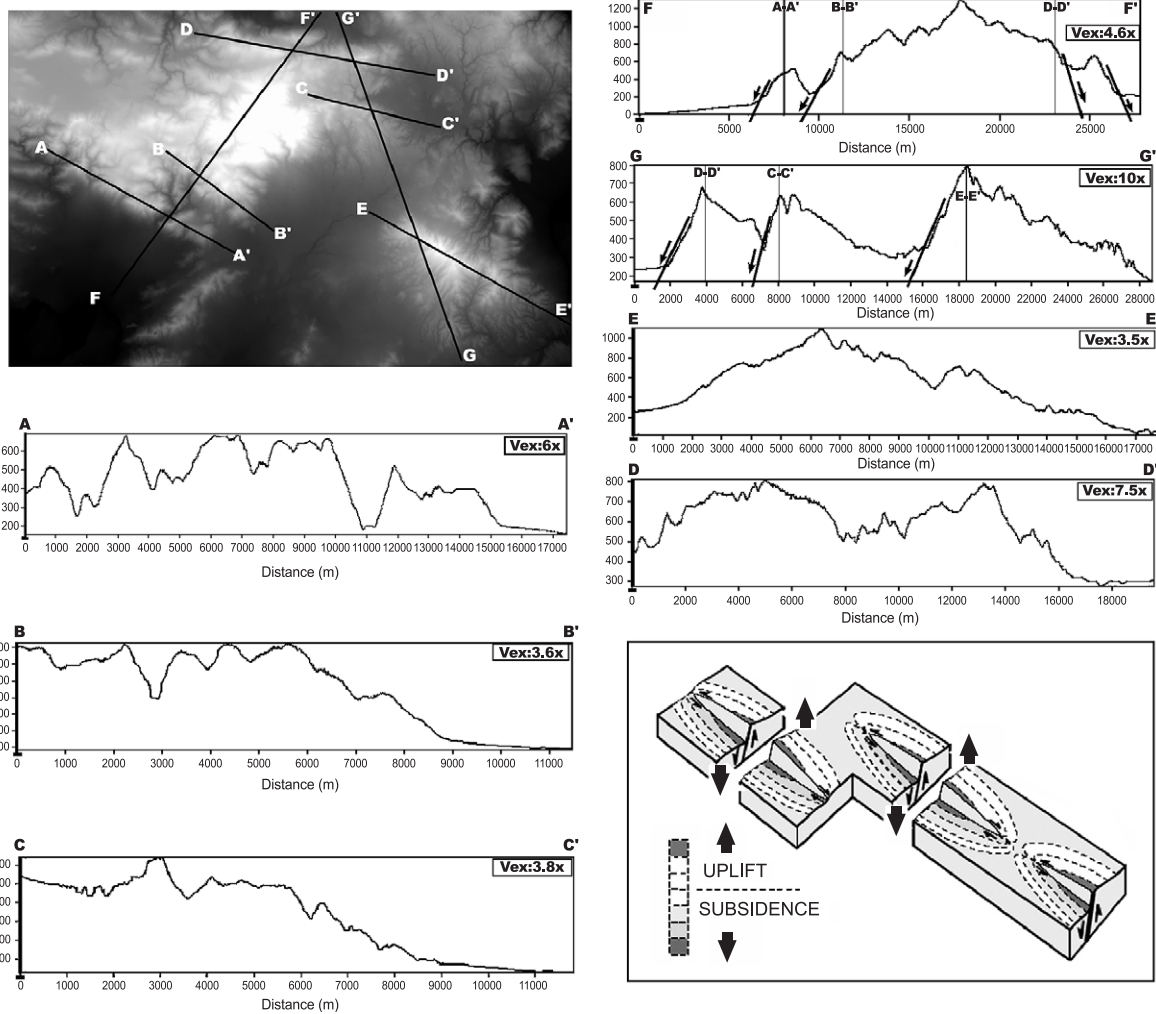
Fig. 5. DEM image of the study area (top left) with profile lines. Five elevation profiles are shown along strike of major normal faults (AA′, BB′, CC′, DD′, and EE′; bottom) and across strike (FF′, GG′; right). Notice the elliptical footwall shape of large segments, Thriassion—AA′, Pendeli—EE′, and Avlon—DD′, as opposed to the asymmetric profile of the small segments (Fili-BB′ and Afidnai-CC′). Thin vertical lines inside dip profiles show intersections with the strike profiles. The vertical axis is exaggerated several times the horizontal axis (see enclosed boxes). Sketch to the bottom right shows cumulative deformation due to normal faulting. Notice that fault displacements die out along the strike of the fault, creating an elliptical profile of the fault plane (Watterson, 1986; Barnett et al., 1987). Not to scale.

escarpments have formed by footwall uplift due to seismic motions (see inset model in Fig. 5), we may calculate fault kinematics. This is done by assuming that bedrock scarp height is a measure of cumulative fault throws inasmuch as offset cannot be determined otherwise on the DEM. It follows that the estimated throw is a minimum because the depth to bedrock in the hanging wall area is unknown. The figures we get are reasonable and can be compared to figures

calculated from published displacement/length ratios of normal faults (Table 1; Schlische et al., 1996; Morewood and Roberts, 2002). Smaller escarpments seen in the transverse profiles are probably due to small normal faults in the interior of the Parnitha Mountain Profile GG′ displays a typical back-tilted terrain due to uplift along AVFS, AFFS, and PEFS and prefaulted flat surfaces in the hanging wall area of AVFS and PEFS.

Table 1
Summary of fault segment morphometry and kinematics

Fault segment	Strike	Length (km)	Relief (m)	Slip (inferred, m)	Age (My)	Slip rate (mm/yr)	Maximum event
Fili (FIFS)	N128E	11	450	381–770	4–5	0.15–0.19	6.4
Pendeli (PEFS)	N116E	18	600	642–1260	8–10	0.13–0.16	6.6
Avlon (AVFS)	N100E	20	700	718–1400	8–10	0.14–0.18	6.6
Thriassion (THFS)	N120E	17	600	604–1190	4–5	0.24–0.30	6.5
Afidnai (AFFS)	N105E	11	350	381–770	4–5	0.15–0.19	6.4

Segments are shown in Fig. 2. Relief is the elevation difference measured from the 20-m DEM. Relief measurements are used to derive minimum throw estimates along normal faults. Displacement values are inferred from Schlische et al., 1996 (left; $d=0.03L^{1.06}$) and Morewood and Roberts, 2002 (right side of column; $d/L=0.07$, mean value for distal normal faults inside the Corinth Rift). Age of faults is taken from the oldest basin fill according to literature. Slip rates are calculated by dividing fault displacement (right side) by age. Maximum earthquake is calculated using the empirical relationship of Pavlides and Caputo (2004).

4.5. Slope profiles of mountain fronts

We constructed slope profiles across the fault segments along the dip-profiles of Fig. 5. We used the slope data shown in Fig. 2b. We found that a marked increase in slope angle occurs as we cross the boundary between the alluvial plain and the mountain front. This is because the boundary line follows large fault scarps, which represent the sum of multiple normal-slip offsets (Figs. 3b and 6). The distribution of the slope data (Fig. 7) suggests that the relationship between scarp height and slope angle can be approximated by a linear fit. As a general behaviour, all profiles slope upwards, indicating increasing angles with scarp height. In order to investigate this tendency with fault position, we also experimented with forms of nonlinear equations (Fig. 8).

Despite the long time-range of escarpment formation in our study area (Pliocene and Quaternary), it is reasonable to expect a systematic relationship between range-front height and slope angle because the locus of seismic strain has not changed through this time period. First, we fitted least-squares regression lines to all five profiles to look for notable differences in our morpho-

logic data sets (Fig. 7). The regression equations have the form $\theta = a \times H + b$ where θ is the slope angle and H is the composite scarp height. The equations are similar for segments Pendeli, Thriassion, and Avlon (PEFS, THFS, and AVFS), while a increases for FIFS and AFFS, respectively. All coefficients of determination (R^2) are greater than 0.47. The large amount of scatter in this plot (Fig. 7) suggests that rupture histories vary among the five range-fronts; however, we may group these data into two subsets, one for the "external" segments (PEFS, THFS, and AVFS) and one for the "internal" segments (AFFS and FIFS). The "internal" segments show larger slope gradients. This may indicate a difference in either (a) larger amount of seismic slip per event relative to the "external" segments or (b) shorter recurrence intervals. Both effects are expected to maintain a steeper slope angle under the same erosion rates during Quaternary. To shed more light into this interesting observation one needs to do further investigation by trenching.

In order to further examine the shape of the profile with fault position, we fitted exponential lines to three of our profiles along the Thriasion, Pendeli, and Avlon fault segments (Fig. 8). These three segments show

Table 2
Morphometry of range-front escarpments in Attica

Fault segment	Scarp base	Scarp top	Base elevation	Top elevation	Height (m)	Distance (m)	Slope angle (°)	N
Pendeli (PEFS)	4216209	4215325	499	849	350	884	21.6	44
Avlon (AVFS)	4231988	4231069	240	602	362	919	21.5	46
Afidnai (AFFS)	4226568	4226388	415	491	76	180	22.8	10
Fili (FIFS)	4217829	4218305	358	559	201	476	22.9	24
Thriassion (THFS)	4215571	4216593	139	555	416	1022	22.1	51

Scarp coordinates are Northings in the Greek projection system (Transverse Mercator projection using the GRS 1980 ellipsoid). Scarp cross-sections are shown in Fig. 5. N—number of measurements.
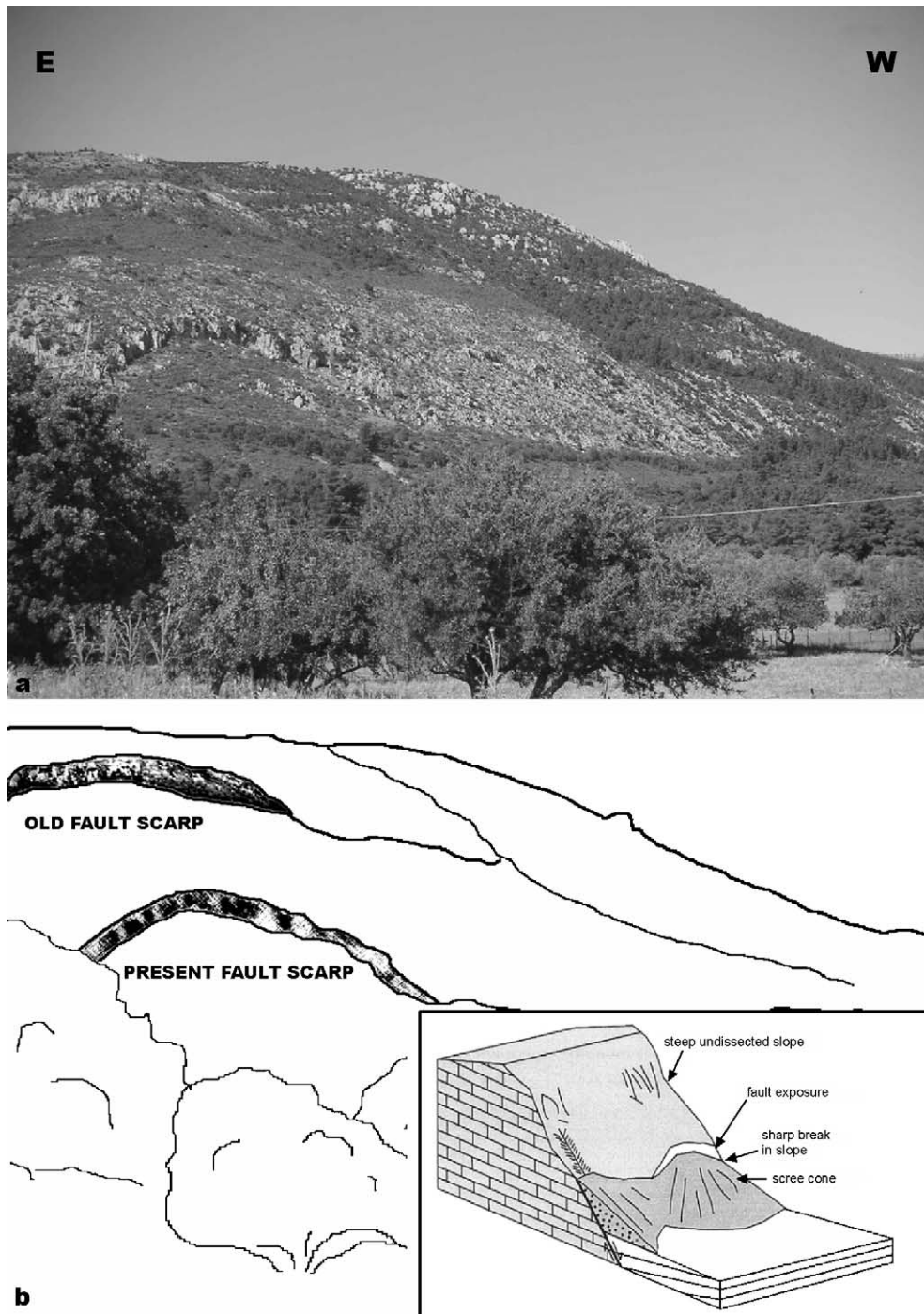
Fig. 6. (a) Field photograph of the Avlon fault escarpment (June 2004) and (b) line drawing of two scarps with the same sense of displacement (down is towards the plain). Locality is the first escarpment along the profile F′F in Fig. 5. Inset sketch at lower right shows a model for the formation of limestone scarps. Not to scale.

Plot of Range-Front Escarpment versus Slope

AFFS: y = 0,4017x + 12,481 R^2 = 0,5794
FIFS: y = 0,1584x + 9,8511 R^2 = 0,4705
AVFS: y = 0,1176x + 14,691 R^2 = 0,4728
PEFS: y = 0,0897x + 17,545 R^2 = 0,5465
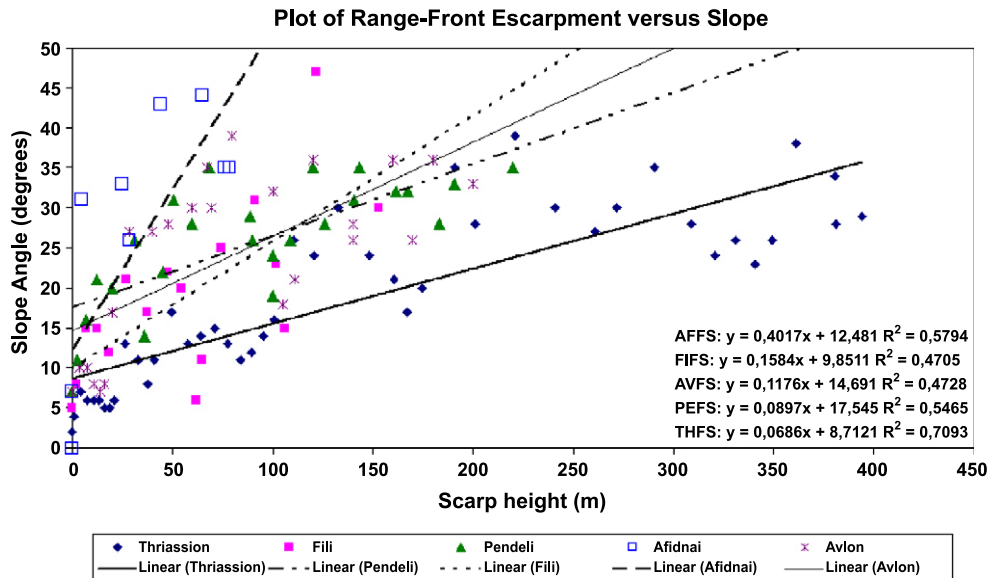THFS: y = 0,0686x + 8,7121 R^2 = 0,7093

Fig. 7. Linear regression plot of range-front heights vs. slope angle data for each segment. Slope angle is the mean value of a 20-m pixel. All fitted lines slope upwards, indicating increased slopes with scarp height. R^2 values indicate goodness of fit and range from 0 to 1.

footwall profiles indicating isolated normal faults (Fig. 5) so footwall uplift may be uniquely linked to individual fault slip. The regression equations have the form $\theta = a - b \times c^H$ where θ is the slope angle and H is the composite scarp height. The goodness of the exponential fit is 0.82 for the Thriassion segment, 0.66 for Pendeli, and 0.72 for the Avlon segment (Fig. 8), much better than the linear fit. The slope angle equation shows an asymptotic behaviour with increasing height. The horizontal asymptote ranges between 30° and 32°, which again indicate that all three segments shared similar slip rates and fault growth history. Moreover, significant breaks on these profiles help us to identify the positions of older bedrock scarps (arrows in Fig. 8). Such an example can be seen along the Avlon segment (Fig. 6) where two scarps occur on the same mountain front. We believe that the nonlinear relationship between escarpment height and slope angle arises from the hanging wall migration of the fault plane, a mechanical process that leads to abandonment of old slip surfaces and is common in the Aegean region (Hancock and Barka, 1987; Stewart and Hancock, 1990; Goldsworthy and Jackson, 2001; Ganas et al., 2004).

A third characteristic of the slope profile is the mean slope angle for each range-front. The angle of all transects across the range-fronts cluster around 22° (Table 2). We suggest that this value is related to (a) the age of the feature (escarpment) and (b) the footwall uplift rates and thus to fault slip rates that range between 0.15 and 0.30 mm/yr (Table 1). The first point is difficult to assess because we do not have good stratigraphic control on the offset synrift across faults, although we believe that all studied escarpments have been in place for at least 2–3 My. The second point gets support from three observations: (a) the fault kinematics indicate similar slip rates (Table 1); (b) the Attica scarps have formed in the same climate; and (c) little scarp degradation occurs because of bedrock lithology (hard Mesozoic limestone; Katsikatsos et al., 1986; Pavlides et al., 2002).

5. Results and discussion

The above analysis of DEM and their derivatives shows where and how we may extract dimensions of fault segments inside rift systems and calculate slip and slip-rate estimates from available data for basin thickness and age. All segments in Northern Attica show geomorphic evidence for recent activity such as

prominent range-front escarpments (Figs. 3 and 6), large slope angle values (Figs. 7 and 8), V-shaped valleys, triangular facets (Fig. 4), and back-tilted
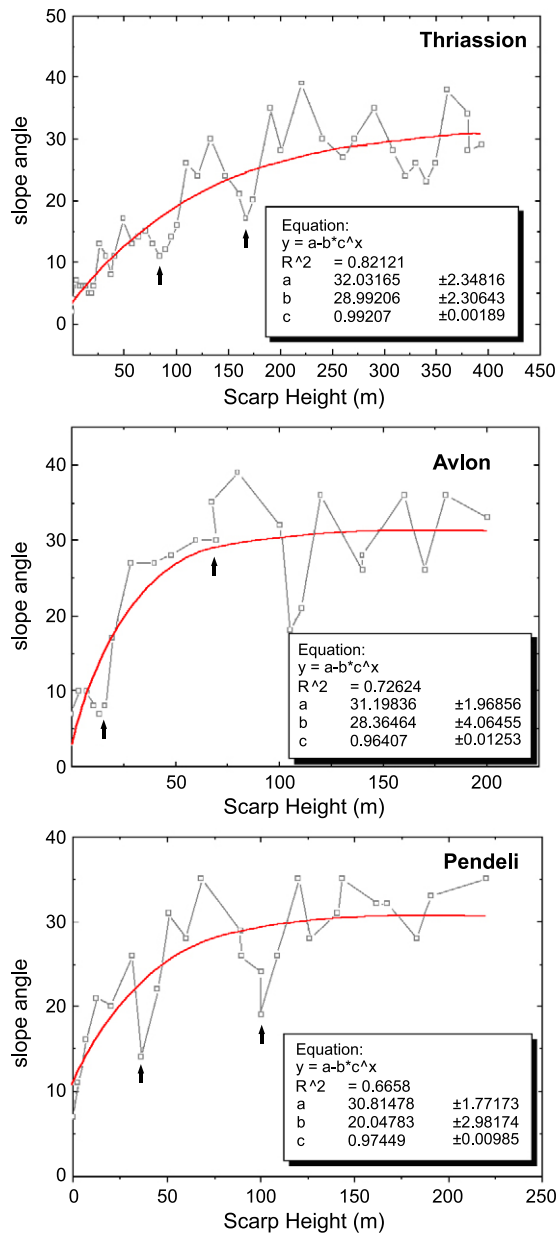

Fig. 8. Exponential regression analysis applied to morphologic data from the Thriassion, Pendeli, and Avlon mountain fronts. Arrows indicate inferred positions of normal fault scarps, where the slope angle first decreases as a relatively flat surface has formed. Notice the asymptotic behaviour of equation for all graphs with horizontal asymptote $30° < y < 32°$.

surfaces (Fig. 5). Table 3 summarizes the image processing techniques used in this study. We were able to confirm that two of the fault segments identified on the DEM (FIFS and AVFS; Fig. 2) were identified as active faults (Ganas et al., 2004; Figs. 3 and 6). Based on the similarity of the geomorphic and kinematic data (Tables 1 and 2), it is reasonable to argue that all five segments are active. We then proceed to calculate maximum earthquake magnitude along all segments, i.e., earthquakes that may rupture the full length of the fault plane. Finally, we suggest that the fault pattern difference seen on the shaded relief image of Attica–Viotia (Fig. 9) is due to Corinth rift propagation to the north of the Parnitha mountain range.

5.1. Maximum earthquakes

We have estimated surface magnitudes (Ms) of future events near Athens from empirical relationships (Table 1). For simplicity, we assume surface rupture lengths (L) equal to the extracted fault lines. The relationships of Ambraseys and Jackson (1998, Ms=$1.14 \times \log L + 5.13$) and Pavlides and Caputo (2004) (Ms=$0.90 \times \log L + 5.48$) supply results with a magnitude difference of 0.1 unit. From our estimates, it is clear that events between 6.4 and 6.6 Ms are to be expected if one of the mapped faults moves. The existence of these fault segments within 20 km of Athens city centre necessitates their further investigation using geological techniques such as trenching to identify previous seismic events and calculate Holocene recurrence intervals.

5.2. Fault segmentation pattern at the end of the Gulf of Corinth Rift and fault slip rates

Another use of DEM imagery emerges when it is compared to focal mechanism data such as those of Fig. 1. We note that both the 1981 earthquake sequence and the 1999 Athens earthquake focal plane solutions match satisfactorily the strike of mountain ranges (Fig. 9) and perhaps the same can be suggested for the 1893 event. This implies that perhaps we could make use of lineaments–fault traces on high-resolution shaded relief images in relation to other geomorphic criteria (facets, etc.) to infer the strike of seismogenic faults inside other rift systems.

Table 3
Summary of image processing techniques and structural interpretation of extracted features

DEM tool	Feature	Landform	Structural interpretation
Tone	Lineament	Escarpment	Normal fault
Slope map	Lineament	Escarpment	Normal fault
Shaded relief	Lineament	Escarpment	Normal fault
Longitudinal elevation profile	Overall curvature	Half dome	Footwall shape
Longitudinal elevation profile	V-shape	Valley	River incision in footwall
Transverse elevation profile	Inclined surface	Escarpment	Footwall relief
Transverse elevation profile	Inclined surface	Tilted surface	Back-tilted prerift
Slope profile across lineament	Ramp	Escarpment	Fault Scarp

The data are presented in Fig. 2 and the profiles in Figs. 5 and 7.

The interpretation of the fault pattern in Fig. 9 (60-m DEM) shows first that the normal faults of Attica are more closely spaced in comparison to the Corinth Rift, further west, a pattern that implies lower slip rates (Cowie and Roberts, 2001). This suggestion may be true because we can calculate mean slip rates for all mapped faults adopting ages for onset of rifting on the basis of geological data (Freyberg, 1951; Mettos et al., 2000; Table 1). Slip rates for the Attica segments range from 0.13 to 0.30, a difference of a factor of two; however, in comparison to the Gulf of Corinth, the difference rises to a factor of 10 to 20 (see Morewood and Roberts, 2002 for a review of Corinth slip rates). The lower slip rates may explain both the long recurrence intervals of earthquakes in Attica and the geomorphic expression that is only a fraction of the huge Quaternary offset across the southern coast of the Gulf of Corinth.

In addition, West Attica is dominated by normal faults striking N60°E to N90°E (Fig. 9), whereas
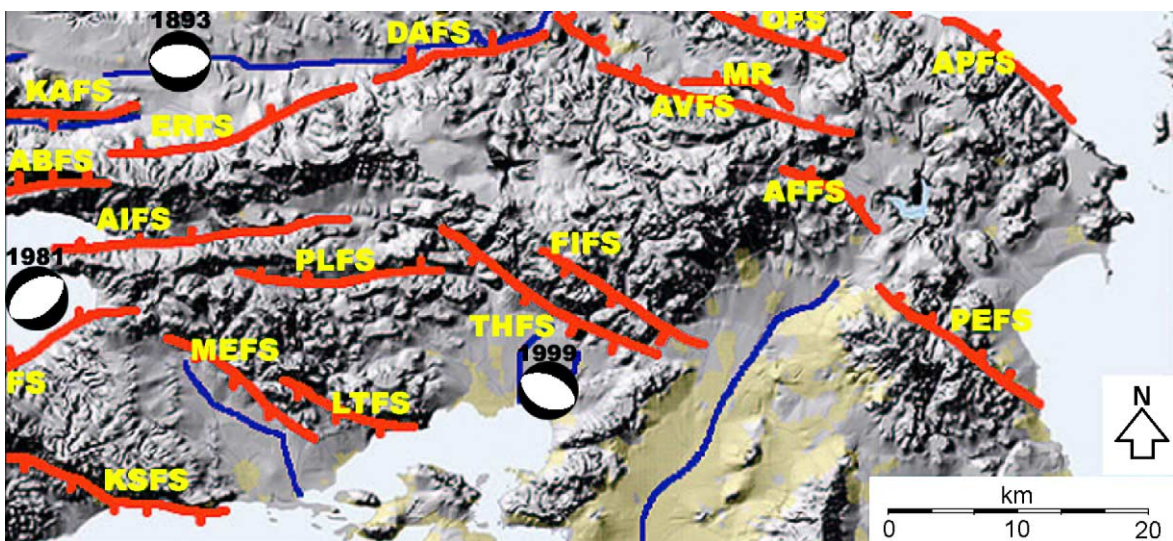

Fig. 9. Structural interpretation of a 60-m relief model of Attica and part of Viotia. The model is illuminated from the North at a low angle to accentuate topography. Red lines are interpreted normal faults. Blue lines are major rivers. Dark yellow pattern indicates urban areas. Note that all faults have lengths less than 20 km, as defined by the systematic reduction of elevations (shadows) towards their ends. APFS Agioi Apostoloi, OFS Oropos, MR Maliza Rupture (Ganas et al., 2004), LTFS Loutropolis, MEFS Megara, KSFS Kakia Skala, PLFS Pyli, AIFS Aigosthena, ABFS Agios Basilios, ERFS Erithres, KAFS Kaparelli, DAFS Dafnoula, segments SAFS, and ERFS have been proposed by Roberts and Ganas (2000); MEFS segment by Goldsworthy and Jackson (2000) (the same authors have named KSFS as Saros Fault); segments THFS and FIFS by Ganas et al. (2001).

both North Attica (Parnitha) and East Attica (Pendeli) is dominated by normal faults striking N120°E (on average; Table 1). NW–SE striking normal faults are also reported by Goldsworthy and Jackson (2002) to occur along the Northern Attica coastline. This marked difference in active fault strikes may be related to the rifting process in central Greece. One scenario is that the Gulf of Corinth rift which is a young 1-Ma structure (Armijo et al., 1996) cannot propagate to the east through Parnitha Mountain, and it has to by-pass it from the north (Fig. 1). It seems reasonable to suggest that the reason for that is the Quaternary volcanism of the area (e.g., Kyriakopoulos et al., 1990; Papazachos and Panagiotopoulos, 1993; Morris, 2000), which has weakened the Attica crust. A soft crust for Attica relative to Viotia has also been inferred by Alessandrini et al. (1997) due to the existence of a low-velocity zone of P-waves. Although the last 300 years may represent a small fraction of recurrence intervals of large earthquakes, we note that no large events have been reported for the West Attica region as opposed to four events>6.0 Ms in Viotia (1853–1893–1914–1938; Fig. 1a). It seems that crustal rheology variations due to volcanic processes has led to stress concentration further north and subsequently, to more effective strain localization inside the stronger plutonic crust of the Viotia region.

6. Conclusions

(1)   We identified five large normal faults in Northern Attica. All of them show geomorphic evidence for recent activity such as prominent range-front escarpments, V-shaped valleys, triangular facets, and tilted footwall areas. Our analysis reveals systematic differences in both escarpment geometry and slope variation. With respect to the fault pattern identified in Fig. 1, we may group these data into two subsets, one for the "external" segments (PEFS, THFS, and AVFS) and one for the "internal" segments (AFFS and FIFS).

(2)   Footwall strike profiles along the "external" segments show elliptical geometry as typical isolated segments, while the "internal" segments show profile asymmetry. This may be due to preexisting topography and/or mechanical interaction between the "external" and "internal" segments.

(3)   The distribution of the slope data (Fig. 7) again suggests a different long-term behaviour between "external" and "internal" segments. The relationship between scarp height and slope angle can be approximated by a linear fit for all; however, the "internal" segments show larger slope gradients. This steepness of the "internal" escarpments may indicate a difference in either (a) larger amount of seismic slip per event or (b) shorter recurrence intervals.

(4)   For all "external" segments, the best fit is nonlinear (Fig. 8), and the slope angle has an asymptote at 30°–32°. This behaviour may arise from the hanging wall migration of the fault plane, a mechanical process that leads to abandonment of old slip surfaces and is common in the Aegean region.

(5)   The mean angles of all range-front escarpments cluster around 22° (Table 2). We suggest that this value is related to fault slip rates that range between 0.13 and 0.3 mm/yr (Table 1). This result may be used as an indicator for fault activity inside other rift systems.

(6)   The 60-m relief image shows a marked difference in fault strikes from west to east across Attica (Fig. 9). This active fault pattern may suggest that strain localization in the upper crust is influenced by rheology variations. The reason for that may be the Quaternary volcanism of western Attica.
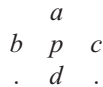
Greece and the General Secretariat for Research and Technology.

Appendix A. Computation of slope angle

For each pixel p=(px, py, pz) we define px and py as the pixel/row location and pz as the elevation. The neighbours of p are a, b, c, d where a=(px, py−1, az), b=(px−1, py, bz), etc.

$$
\begin{matrix}
& a & \\
b & p & c \\
. & d & .
\end{matrix}
$$

We calculate the slope angle as follows:

(1) Define two vectors, **V1** and **V2**, across the pixel p (left to right) and (top to bottom)

$$\mathbf{V1} = (dx,0,dzx)$$

$$= (2*PXSZ(1),0,(bz - cz)*ELSZ)$$

$$\mathbf{V2} = (0,dy,dyz)$$

$$= (0,2*PXSZ(2),(az - dz)*ELSZ)$$

where dzx and dzy are the elevation changes between pixels, and dx and dy are the projected distances between pixels. PXSZ and ELSZ are parameters specified by the user giving pixel ground size and elevation sizes. dx and dy will be twice the actual pixel ground size inasmuch as the elevation differences (or gradients) are taken over 2-pixel distances.

(2) Find the normal vector to the plane formed by the two vectors **V1** and **V2**, by taking the cross product:
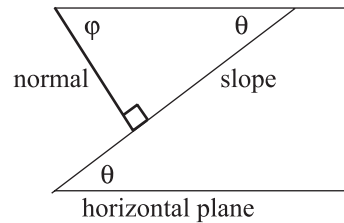
$$N = \mathbf{V1} \times \mathbf{V2} = (- dy*dzx, - dx*dzy, dx*dy)$$

$$= nx,ny,nz$$

(3) The sine of the angle φ between the normal vector and horizontal plane is calculated as:

$$\sin(angle) = \frac{nz}{\sqrt{nx^2 + ny^2 + nz^2}}$$

(4) From trigonometry: slope of plane $\theta=90-\varphi$ (slope of normal), thus the slope angle for the pixel can be calculated as

$$slope = \arccos \frac{nz}{\sqrt{nx^2 + ny^2 + nz^2}}$$

References

Alessandrini, B., Beranzoli, L., Drakatos, G., Falcone, C., Karantonis, G., Mele, F.M., Stavrakakis, G., 1997. Back arc basins and P-wave crustal velocity in the Ionian and Aegean regions. Geophysical Research Letters 24, 527–530.

Ambraseys, N.N., Jackson, J.A., 1990. Seismicity and associated strain of central Greece between 1890 and 1988. Geophysical Journal International 101, 663–708.

Ambraseys, N.N., Jackson, J.A., 1997. Seismicity and strain in the Gulf of Corinth (Greece) since 1694. Journal of Earthquake Engineering 1, 433–474.

Ambraseys, N.N., Jackson, J.A., 1998. Faulting associated with historical and recent earthquakes in the Eastern Mediterranean region. Geophysical Journal International 133, 390–406.

Anders, M.H., Schlische, R.W., 1994. Overlapping faults, intrabasin highs, and the growth of normal faults. Journal of Geology 102, 165–180.

Armijo, R., Meyer, B., King, G.C.P., Rigo, A., Papanastassiou, D., 1996. Quaternary evolution of the Corinth Rift and its implications for the Late Cenozoic evolution of the Aegean. Geophysical Journal International 126, 11–53.

Barnett, J.A.M., Mortimer, J., Rippon, J.H., Walsh, J.J., Watterson, J., 1987. Displacement geometry in the volume containing a single normal-fault. AAPG Bulletin of the American Association of Petroleum Geologists 71, 925–937.

Clarke, P.J., Davies, R.R., England, P.C., Parsons, B., Billiris, H., Paradissis, D., Veis, G., Cross, P.A., Denys, P.H., Ashkenazi, V., Bingley, R., Kahle, H.G., Muller, M.V., Briole, P., 1998. Crustal strain in central Greece from repeated GPS measurements in the interval 1989–1997. Geophysical Journal International 135, 195–214.

Cowie, P.A., Roberts, G.P., 2001. Constraining slip rates and spacings for active normal faults. Journal of Structural Geology 23, 1901–1915.

Drakatos, G., Melis, N., Papanastassiou, D., Karastathis, V., Papadopoulos, G.A., Stavrakakis, G., 2002. 3-D crustal velocity structure from inversion of local earthquake data in Attiki (central Greece) region. Natural Hazards 27, 1–14.

Duncan, C., Masek, J., Fielding, E., 2003. How steep are the Himalaya? Characteristics and implications of along-strike topographic variations. Geology 31, 75–78.

Freyberg, V.B., 1951. Das Neogen gebiet nordwestlich Athen. Subsurface Research Department, Ministry of Coordination, Special Publication, vol. 1, pp. 85–86.

Ganas, A., 1997. Fault segmentation and seismic hazard assessment in the Gulf of Evia rift, central Greece. PhD thesis, The University of Reading, Reading, UK.

Ganas, A., 2002. Methods for imaging earthquake deformation using satellite data and digital elevation models. In: Gorur, N., et al., (Eds.), Integration of Earth Science Research on the Turkish and Greek 1999 Earthquakes. Kluwer Academic Publishers, pp. 197–204.

Ganas, A., Papadopoulos, G., Pavlides, S.B., 2001. The 7th September 1999 Athens 5.9 Ms earthquake: remote sensing and digital elevation model inputs towards identifying the seismic fault. International Journal of Remote Sensing 22, 191–196.

Ganas, A., Pavlides, S.B., Valkaniotis, S., Sboras, S., Papaioannou, S., Alexandris, G.A., Plessa, A., Papadopoulos, G.A., 2004. Active fault geometry and kinematics in Parnitha Mountain, Attica, Greece. Journal of Structural Geology 26, 2103–2118.

Goldsworthy, M., Jackson, J., 2000. Active normal fault evolution in Greece revealed by geomorphology and drainage patterns. Geological Society Journal 157, 967–981.

Goldsworthy, M., Jackson, J., 2001. Migration of activity within normal fault systems: examples from the Quaternary of mainland Greece. Journal of Structural Geology 23, 489–506.

Goldsworthy, M., Jackson, J., Haines, J., 2002. The continuity of active fault systems in Greece. Geophysical Journal International 148, 596–618.

Hancock, P.L., Barka, A.A., 1987. Kinematic indicators on active normal faults in western Turkey. Journal of Structural Geology 9, 573–584.

Hellenic Army Geographical Service, 1978. 1:250,000 Map Sheet "Khalkis".

Hellenic Army Geographical Service, 1988. 1:50,000 Map Sheet "Kifisia".

Hellenic Army Geographical Service, 1992. 1:50,000 Map Sheet "Elefsis".

Holmes, K.W., Chadwick, O.A, Kyriakidis, P.C., 2000. Error in a USGS 30-meter digital elevation model and its impact on terrain modeling. Journal of Hydrology 233, 154–173.

Hooper, D.M., Bursik, M.I., Webb, F.H., 2003. Application of high-resolution interferometric DEMs to geomorphic studies of fault scarps, Fish Lake Valley, Nevada–California, USA. Remote Sensing Environment 84, 255–267.

Jackson, J., Leeder, M., 1994. Drainage systems and the development of normal faults: an example from Pleasant Valley, Nevada. Journal of Structural Geology 16, 1041–1959.

Jordan, G., Csillag, G., Szucs, A., Qvarfort, U., 2003. Application of digital terrain modelling and GIS methods for the morpho-tectonic investigation of the Kali Basin, Hungary. Zeitschrift Fur Geomorphologie 47, 145–169.

Katsikatsos, G., 1977. La structure tectonique d' Attique et l' île d' Eubee. Proceedings Vth Coll. On the Aegean Region, vol. 1. IGME Publications, Athens, pp. 211–228.

Katsikatsos, G., Mettos, A., Vidakis, M., Dounas, A., 1986. Geological map of Greece 1:50,000 Athens—Elefsis Sheet, IGME, Athens.

Kyriakopoulos, K.G., Kanarissotiriou, R., Stamatakis, M.G., 1990. The authigenic minerals formed from volcanic emanations at Soussaki, west Attica peninsula, Greece. Canadian Mineralogist 28, 363–368.

Leeder, M.R., Jackson, J.A., 1993. The interaction between normal faulting and drainage in active extensional basins, with examples from western United States and central Greece. Basin Research 5, 79–102.

Mariolakos, I., Foudoulis, I., Sideris, C., Chatoupis, T., 2001. The morphotectonic structure of Parnis Mt. (Attica, Greece). Bulletin of the Geological Society of Greece 34, 183–190.

Menges, C.M., 1990. Late Quaternary fault scarps, mountain-front landforms, and Pliocene–Quaternary segmentation on the range-bounding fault zone, Sangre de Cristo Mountains, New Mexico. In: Krinitzsky, E.L., Slemmons, D.B (Eds.), Neotectonics in Earthquake Evaluation, vol. 8. Geological Society of America Reviews in Engineering Geology, Boulder, Colorado, pp. 131–156.

Metaxas, C., Angelopoulos, A., Lalechos, S., Foundoulis, D., 2001. Deep tectonic structure of northwestern Attica, Greece: geodynamic pattern of Athens earthquake. Bulletin of the Geological Society of Greece 34, 259–265.

Mettos, A., Ioakim, Ch., Rondoyanni, Th., 2000. Palaeoclimatic and palaeogeographic evolution of Attica–Beotia (Central Greece). Special Publication - Geological Society of Greece, vol. 9, pp. 187–196.

Michetti, A.M., Ferreli, L., Esposito, E., Porfido, S., Blumetti, A.M., Vittori, E., Serva, L., Roberts, G.P., 2001. Ground effects during the 9 September 1998, Mw=5.6, Lauria earthquake and the seismic potential of the "aseismic" Pollino Region in Southern Italy. Seismological Research Letters 71, 31–46.

Morewood, N.C., Roberts, G.P., 2002. Surface observations of active normal fault propagation: implications for growth. Journal of the Geological Society 159, 263–272.

Morris, A., 2000. Magnetic fabric and palaeomagnetic analyses of the Plio-Quaternary calc-alkaline series of Aegina Island, South Aegean volcanic arc, Greece. Earth and Planetary Science Letters 176, 91–105.

Murphy, W., 1993. Remote Sensing of active faults: case studies from southern Italy. Z. Geomorphol. N. F., Suppl. Bd. 94, 1–23.

Oguchi, T., Aoki, T., Matsuta, N., 2003. Identification of an active fault in the Japanese Alps from DEM-based hill shading. Computers & Geosciences 29, 885–891.

Papadopoulos, G.A., 2000. Historical earthquakes and tsunamis in the Corinth Rift, Central Greece. Publication, vol. 12. National Observatory of Athens, Institute of Geodynamics, Athens.

Papadopoulos, G.A., Drakatos, G., Papanastassiou, D., Kalogeras, I., Stavrakakis, G., 2000. Preliminary results about the catastrophic earthquake of 7 September 1999 in Athens, Greece. Seismological Research Letters 71, 318–329.

Papazachos, B.C., Panagiotopoulos, D.G., 1993. Normal faults associated with volcanic activity and deep rupture zones in the southern Aegean volcanic Arc. Tectonophysics 220, 301–308.

Pavlides, S., Caputo, R., 2004. Magnitude versus faults' surface parameters: quantitative relationships from the Aegean Region. Tectonophysics 380, 159–188.

Pavlides, S.B, Papadopoulos, G., Ganas, A., 2002. The fault that caused the Athens September 1999 Ms=5.9 earthquake: field observations. Natural Hazards 27, 61–84.

Pike, R.J., 2000. Geomorphometry—diversity in quantitative surface analysis. Progress in Physical Geography 24, 1–20.

Roberts, G.P., Ganas, A., 2000. Fault-slip directions in central and southern Greece measured from striated and corrugated fault planes: comparison with focal mechanism and geodetic data. Journal of Geophysical Research 105, 23443–23462.

Roberts, G.P., Michetti, A.M., Cowie, P., Morewood, N.C., Papanikolaou, I., 2002. Fault slip-rate variations during crustal-scale strain localisation, central Italy. Geophysical Research Letters 29, 1168, doi:10.1029/2001GL013529.

Robertson, A.H.F., Clift, P.D., Degnan, P.J., Jones, G., 1991. Tectonic evolution of the Mesozoic—Cenozoic Pindos Ocean: Greece. Bulletin of the Geological Society of Greece 25, 55–64.

Salvi, S., 1995. Analysis and interpretation of Landsat synthetic stereo pair for the detection of active fault zones in the Abruzzi region (central Italy). Remote Sensing of Environment 53, 153–163.

Sanders, C.O., Slemmons, D.B., 1996. Geomorphic evidence for Holocene earthquakes in the Olinghouse fault zone, Western Nevada. Bulletin of the Seismological Society of America 86, 1784–1792.

Schlische, R.W., Young, S.S., Ackermann, R.V., Gupta, A., 1996. Geometry and scaling relations of a population of very small rift-related normal faults. Geology 24, 683–686.

Stewart, I.S., Hancock, P.L., 1990. Brecciation and fracturing within neotectonic normal fault zones in the Aegean region. In: Knipe, R.J., Rutter, E. (Eds.), Deformation Mechanisms, Rheology and Tectonics, Special Publication - Geological Society of London, vol. 54, pp. 105–112.

Taymaz, T., Jackson, J., McKenzie, D., 1991. Active tectonics of the north and central Aegean Sea. Geophysical Journal International 106, 433–490.

Vysotsky, E.M., Vishnevskaya, E.A., Elobogoev, A.V., 2002. Neotectonic analysis of northern Lake Teletskoe using digital elevation modeling. Geologiya i Geofizika 43, 1099–1106.

Watterson, J., 1986. Fault dimensions, displacements and growth. Pure and Applied Geophysics 124, 365–373.

Wdowinski, S., Zilberman, E., 1997. Systematic analyses of the large-scale topography and structure across the Dead Sea Rift. Tectonics 16, 409–424.